Supplementary Information

Significantly enhanced photocurrent for water oxidation in monolithic Mo:BiVO$_4$/SnO$_2$/Si by thermally increasing the minority carrier diffusion length

Liming Zhang[†], Xiaofei Ye[†], Madhur Boloor, Andrey Poletayev, Nicholas A. Melosh,

William C. Chueh[*]

[*]Corresponding Author, wchueh@stanford.edu

Chemicals

Sulfuric acid (H_2SO_4, 98%) and hydrogen peroxide (H_2O_2, 30%) were purchased from Fisher Scientific. Tin oxide (SnO_2) (powder, 99.9%), antimony trioxide (Sb_2O_3) (powder, 99.99%), bismuth (III) nitrate pentahydrate ($Bi(NO_3)_3$ $5H_2O$, $\geq$ 99.99%), vanadyl (IV) acetylacetonate (VO $(acac)_2$, $\geq$ 99.98%), bis(acetylacetonato) dioxomolybdenum (VI) ($MoO_2(acac)_2$, $\geq$ 99.99%), p-benzoquinone ($C_6H_4(=O)_2$, $\geq$ 98%), potassium phosphate monobasic (KH_2PO_4, $\geq$ 99.95%), potassium phosphate dibasic (K_2HPO_4, $\geq$ 99.95%), potassium iodide (KI, $\geq$ 99%), nitric acid (HNO_3, 68.0-70.0%), dimethyl sulfoxide (DMSO, $\geq$ 99.9%), glacial acetic acid (CH_3CO_2H, $\geq$ 99.5%), titanium isopropoxide (TTIP, 97%), hydrochloric acid (HCl, 36.5-38%), sodium sulfite (Na_2SO_3, $\geq$ 98%), sodium sulfate (Na_2SO_4, $\geq$ 98%), cobalt (II) nitrate hexahydrate ($Co(NO_3)_2$ $6H_2O$, $\geq$ 98%), potassium hexachloroiridate (III) (K_3IrCl_6, $\geq$ 99.9%) and potassium hexachloroiridate (IV) (K_2IrCl_6, $\geq$ 99.9%) were purchased from Sigma Aldrich. All chemicals were used as purchased. Solutions were prepared using high purity water (Millipore Milli-Q purification system, resistivity $\geq$ 18.2 M$\Omega\cdot$cm). Glass wafers coated with fluorine-doped tin oxide (FTO) were purchased from MTI.

Preparation of CoPi/Mo:BiVO$_4$/SnO$_2$/Si electrodes

Before deposition, an n-type Si wafer (<100> orientation, 1-5 $\Omega\cdot$cm, WRS materials) was immersed in a piranha solution (H_2SO_4:H_2O_2, 2:1) at 90 ^{o}C for 15 min and then dipped in 50:1 HF for 2 min to remove the native oxide. The wafer was thoroughly rinsed with DI water and dried under gentle N_2 flow. After cleaning, the wafer was

immediately transferred into a vacuum chamber for pulsed-laser deposition (PLD, PLD/MBE-2300, PVD Products). Prior to deposition, the Si substrate was first annealed at 600 °C in 230 mTorr O_2 for 10 min in order to form a thin oxide passivation layer. An Sb-doped SnO_2 (Sb:SnO_2) thin film was then deposited by PLD at 350 °C in 40 m Torr O_2. The thickness of Sb:SnO_2 is not expected to be a critical issue, since it is a degenerate film and working as a metallic layer (confirmed to form a Schottky junction with Si and an ohmic junction with $BiVO_4$). To prevent the formation of pinholes, the typical thickness of Sb:SnO_2 film was ~110 nm. A KrF (248 nm) excimer laser was used to ablate the target at a fluency of 1 J cm^{-2} and a repetition rate of 10 Hz. The substrate-to-target distance was kept at 100 mm. The ablation targets were fabricated using a solid-state reaction method, where SnO_2 powder was mixed with Sb_2O_3 powder (6 wt.%), pressed uniaxially at 140 MPa and then sintered in 21% O_2 balanced with Ar at 1300 °C for 10 h.

To synthesize nanoporous $BiVO_4$, a 0.04 mol L^{-1} $Bi(NO_3)_3$ solution was prepared by dissolving $Bi(NO_3)_3$ $5H_2O$ in a 50 mL of 0.40 mol L^{-1} KI solution after adjusting the pH to 1.7 by adding HNO_3. This solution was mixed with 20 mL of pure ethanol containing 0.23 mol L^{-1} p-benzoquinone in the electrochemical cell. A three-electrode electrochemical cell was used for the electrodeposition with a SnO_2/Si substrate working electrode (WE), Ag/AgCl (1M NaCl) reference electrode (RE) and a platinum (Pt) counter electrode (CE). For electrodeposition and subsequent electrochemical characterizations, a Biologic SP-300 potentiostat was used. Cathodic deposition was performed potentiostatically at -0.10 V *vs*. Ag/AgCl at room temperature (RT). After

electrodeposition, a uniform orange bismuth oxyiodide (BiOI) film was obtained on the SnO$_2$/Si substrate. Next, a 0.07-0.20 mL DMSO solution containing 0.20 mol L^{-1} VO(acac)$_2$ was drop-cast onto the BiOI film and heated in a muffle furnace at 450 °C, at a ramping rate of 2 °C min^{-1}, for 2 h to obtain BiVO$_4$. Mo-doping was achieved by adding different amounts of 0.20 mol L^{-1} MoO$_2$(acac)$_2$ in DMSO to a VO(acac)$_2$/DMSO solution. After annealing, excess V$_2$O$_5$ remaining on the BiVO$_4$ electrodes was removed by soaking in a 1 M NaOH aqueous solution for 30 s with gentle stirring. The resulting Mo:BiVO$_4$/SnO$_2$/Si electrodes were rinsed with DI water and dried at RT. X-ray diffraction confirmed the monoclinic and tetragonal phase of Mo:BiVO$_4$ and SnO$_2$, respectively (Figure S1), and image analysis showed that the Mo:BiVO$_4$ has an average particle size of ~110 nm (Figure S2a).

A cobalt phosphate (CoPi) catalyst layer was photo-electrodeposited onto Mo:BiVO$_4$ electrodes using a procedure modified from previously reported protocols.[1, 2] A three-electrode cell was used with Mo:BiVO$_4$/SnO$_2$/Si, Ag/AgCl and Pt wire as the WE, RE and CE, respectively. A CoPi film was deposited potentiostatically at 0.0 V *vs.* Ag/AgCl in a solution of 0.15 mM Co(NO$_3$)$_2$ in a 0.1 M phosphate buffer solution (pH 7) for 600 s under 1 sun illumination. The loading of CoPi was optimized by controlling the electrical charge passed per geometric area. The obtained CoPi film was rinsed with excess DI water and dried under gentle N$_2$ flow.

Synthesis of macroporous Mo:BiVO$_4$

For the synthesis of macroporous Mo:BiVO$_4$, Bi(NO$_3$)$_3$ 5H$_2$O in glacial acetic acid (0.20 mol L^{-1}) and VO(acac)$_2$ in DMSO (0.02 mol L^{-1}) were used as precursors, and MoO$_2$(acac)$_2$ in DMSO (0.01 mol L^{-1}) was added for Mo doping. The solution was drop-cast onto FTO substrates (25-100 μL cm^{-2} for varying the thickness), dried in air, and finally calcined at 450 °C (at a ramping rate of 2 °C min^{-1}) in air for 2 h. Image analysis showed that this Mo:BiVO$_4$ has an average particle size of ~275 nm (Figure S2b).

Optimization of nanoporous Mo:BiVO$_4$

To optimize the morphology, nanoporous Mo:BiVO$_4$ was directly synthesized on the FTO substrate using the same procedure described above. To maximize photoactivity and eliminate the majority carrier transport resistance, Mo:BiVO$_4$ was synthesized with different doping levels and film thicknesses by adding different amounts of MoO$_2$(acac)$_2$ and applying varied electrodeposition time, respectively. Raman spectroscopy indicated that the Raman shift of the V-O stretching mode varies linearly with the nominal doping level (Figure S3), confirming that Mo was incorporated into BiVO$_4$.[3] Photocurrent measurement revealed that the 1.0 mol% Mo doping level gave the highest photocurrent (Figure S4). At lower doping levels, majority carrier conductivity presumably limits the photocurrent, whereas at higher doping levels, the performance may be limited by the increased dopant-induced recombination. In order to optimize the thickness of Mo:BiVO$_4$ electrode, the film thickness was controlled by varying the deposition time of BiOI precursor from 30 s to 4 min. As shown in Figure

S5, the cross-sectional SEM images were used to evaluate the thickness of the porous Mo:BiVO$_4$ films. Figure S6 shows the photocurrent (at 1.23 V *vs.* RHE) under both front and back illuminations (through the electrolyte, and through the transparent substrate, respectively). The photocurrent under front illumination reached the maximum value for a film thickness of approximately 630 nm (1 min deposition). Since this film thickness is greater than the optical penetration depth for BiVO$_4$, light absorption does not limit the photocurrent. For example, 90% of photons with wavelength smaller than 450 nm was absorbed (Figure S7). For thinner films, light absorption limits the photocurrent. Comparing the photocurrent under front and back illumination reveals possible majority carrier transport limitations.

Hydrothermal TiO$_2$ nanowire array growth

TiO$_2$ nanowire photoelectrodes were prepared by growing nanowire arrays on FTO.[4, 5] DI water (5 mL) was mixed with HCl (5 mL 36.5-38%) and stirred for 5 min before TTIP (0.167 mL) was added. After stirring for 4 h, the mixture was transferred to a Teflon-lined stainless steel autoclave. Clean FTO/glass substrates were immersed with the conducting side face down. The autoclave was put in an oven at a temperature of 200 °C and was taken out from the oven after 2.5 h. After the autoclave was cooled to room temperature, the FTO substrate was rinsed with DI water and subsequently annealed at 400 °C for 2 h in air. X-ray diffraction confirmed that the as-deposited film was in tetragonal rutile phase. As shown in Figure S20b, the (002) diffraction peak was significantly enhanced, which indicates that the film is highly oriented with respect to

the FTO surface, consistent with the morphology shown in the SEM image (Figure S20a).

Photoelectrochemical (PEC) characterization

The PEC characterization was carried out in a homemade temperature-controlled cell (Figure S8a), which was immersed in a water bath connected to a thermostatic circulator. The cell temperature was measured via a Teflon-coated thermocouple located adjacent to the electrode, and the typical variation for a given temperature set point was ± 0.5 °C. A small thermocouple was mounted on the back of the monolithic photoelectrode, as well as placed in the electrolyte a few mm away from the sample. As shown in Figure S8b, after irradiation for more than 10 hours, the electrode and electrolyte temperatures differ by no more than ± 1 ^{o}C under all temperatures. The good temperature uniformity is attributed to the small electrode area under irradiation (0.28 cm^2), relative to the large volume of the electrolyte (approximately 50 mL), which is stirred throughout the experiments. Photocurrent measurements were carried out using a solar simulator (350 to 1,100 nm, HAL-320, Asahi Spectra Inc.), the spectrum of which has been verified by a UV-vis spectrometer (USB 2000+, Ocean Optics). The illumination intensity was calibrated to achieve a 1 sun condition (79 mW cm^{-2} in the wavelength range of 350 to 1,100 nm). The light entered the cell through a quartz window with an illuminated area of 0.28 cm^2. A Pt wire and a reversible hydrogen electrode (RHE, eDAQ Inc.) were used as the CE and RE, respectively. The WE was sealed by an o-ring in the homemade cell and the electrolyte was purged with Ar for 20 min before and during each

measurement. Most of the photocurrent measurements in this work were conducted in a 0.5 M phosphate buffer solution (pH 7). For the photoelectrode stability and gas chromatography characterization, a 0.5 M Na_2SO_4 aqueous solution (pH 7) was used. The photoactivity of the tandem electrode in the sulfate electrolyte is slightly lower than that in the phosphate buffer solution due to the inability of CoPi to self-regenerate[6, 7] (Figure S9). To address the mass transference problem in the neutral electrolyte, a membrane-free system with stirring was employed.[8] Photocurrents of TiO_2 nanowire electrodes were measured in a 1 M NaOH aqueous solution (pH 14). In some experiments, 0.1 M Na_2SO_3 was added to the electrolyte as a hole-scavenger to speed up the kinetics of the reaction at the electrode/electrolyte interface.

Incident photon-to-current conversion efficiency (IPCE) measurement

For the IPCE measurement, the solar simulator was coupled with a monochromator (CMS-100, Asahi Spectra Inc.) to sweep the wavelength of incident light. IPCE was measured by varying the wavelength of a small-magnitude monochromatic light superimposed onto another background light via a 50:50 beam splitter (Figure S16). The overall incident light spectrum and intensity were verified by a UV-vis spectrometer. The IPCE was then calculated from the photocurrent measured at 0.60 V *vs.* RHE, according to the following equation:

$$IPCE = \frac{J_{ph}(mA\ cm^{-2}) \times 1239.8\ (V\ nm)}{P_{mono}(mW\ cm^{-2}) \times \lambda\ (nm)}$$

We also determined the theoretical saturation photocurrent density, $J_{max} = 6.25$ mA cm^{-2}, by assuming 100% IPCE for photons with energy larger than the experimentally measured band gap (2.59 eV, Figure S7). Further considering the experimentally measured light absorption efficiency (Figure S7), the maximum current density $J_{abs} = 4.67$ mA cm^{-2}.

Gas measurement

Product gas was quantified by on-line gas chromatography. The experiment was conducted in a gas-tight cell containing a 0.5 M Na$_2$SO$_4$ (pH 7) aqueous solution. The content of the cell was vigorously stirred and high purity N$_2$ (99.999%, Praxair) was purged at a constant rate of 1 sccm using a mass flow controller. Potentiostatic electrolysis was conducted at an applied potential of 0.50 V *vs.* RHE for 5 h at each temperature. The outflowing gas was collected and passed into the sampling loop of a gas chromatography (Trace GC Ultra, Thermo Scientific). The measured oxygen concentration was corrected for the presence of a small air impurity, the concentration of which was verified before and after each measurement. To achieve a steady state, we waited for 3 h before analyzing the gas (Figure S17). Nearly stoichiometric O$_2$ and H$_2$ were detected, with a Faradaic efficiency of nearly 90%, both essentially independent of temperature (Table S1).

Photocurrent simulation with different minority carrier diffusion length and depletion layer thickness

The behavior of a wide-bandgap photoanode for water oxidation was modeled by Butler by treating the semiconductor-electrolyte interface as a Schottky junction.[9] In the limit of non-limiting reaction kinetics, the wavelength-dependent photocurrent J, as a function of applied bias V, can be described by the following equation:

$$J^{(\lambda)} = q\, \varphi_0^{(\lambda)} \left\{ 1 - \frac{\exp\left[-\, \alpha^{(\lambda)} \times W_0 \times (V - V_{fb})^{1/2}\right]}{1 + \alpha^{(\lambda)} \times L_D} \right\}$$

where $\varphi_0^{(\lambda)}$ and $\alpha^{(\lambda)}$, are the photon flux and the optical absorption coefficient at certain wavelength, respectively. V_{fb}, W_0 and L_D are flat-band potential, width of the space charge region, and minority carrier diffusion length, respectively. The total photocurrent under simulated sunlight is the integration at all wavelengths. In the case of Fe_2O_3, L_D is 2-4 nm[10], smaller than W_0 (~10 nm), and therefore the photocurrent does not increase much with improved L_D. This is confirmed from the simulation (Figure S18a, solid lines), assuming a constant $\alpha = 10^5$ cm^{-1}, for all above band-gap photons. If we increase L_D to be much larger than W_0 in the simulation (L_D = 70-130 nm, dashed lines), the photocurrent is indeed more sensitive to the improvement in L_D. The latter appropriately describes the significant thermal enhancement in $BiVO_4$ photoanode as its minority carrier diffusion length (~100 nm) is much larger than the width of the space charge region (~10 nm).[11, 12]


Open-circuit potential (OCP) measurement

The OCP was measured in a 0.5 M phosphate buffer solution containing a 0.10 mM $[IrCl_6]^{2-}$/1.0 mM $[IrCl_6]^{3-}$ reversible redox couple (pH 7) under 1 sun illumination. A

PEC cell with a very thin electrolyte film (<5 mm) was used to eliminate the light absorption from the yellow-colored electrolyte containing the reversible redox couple.

Thermally-activated electrocatalysis

To study the temperature effect on the electrocatalysis at the electrode/electrolyte interface, a CoPi catalyst layer was electrodeposited onto FTO and Mo:BiVO$_4$/FTO using a previously reported protocol with modified conditions.[13, 14] A three-electrode cell was used with FTO (Mo:BiVO$_4$/FTO), Ag/AgCl and Pt wire as the WE, RE and CE, respectively. A CoPi film was deposited potentiostatically at 1.1 V *vs.* Ag/AgCl in a solution of 0.15 mM Co(NO$_3$)$_2$ in a 0.1 M phosphate buffer solution (pH 7) for 600 s. To study the kinetic contributions, we examined the electrocatalytic activity as a function of temperature in the dark. As shown in the linear sweep voltammograms and Tafel plots (Figure S19), the activity of the electrocatalyst increases with temperature. The thermal activation energies at an overpotential of 0.60 V are similar for CoPi/FTO and CoPi/Mo:BiVO$_4$/FTO, which are 0.21 $\pm$ 0.02 and 0.20 $\pm$ 0.01 eV, respectively.

Figures
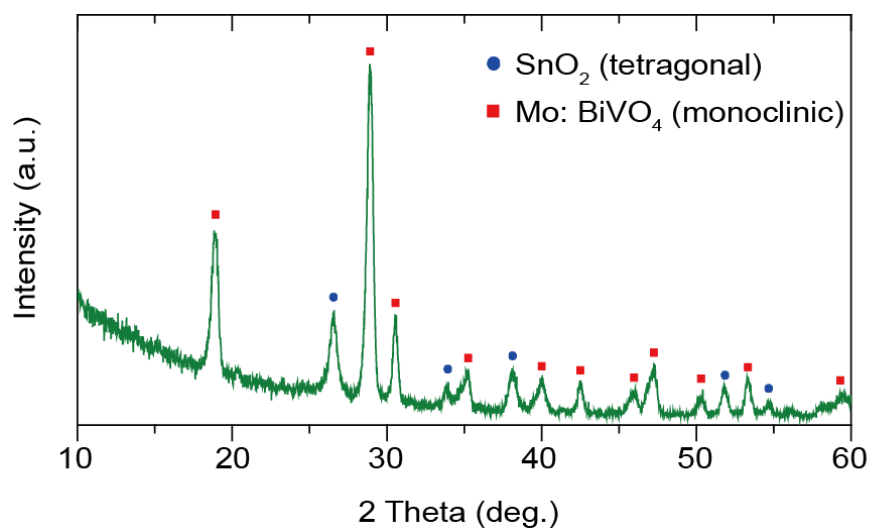
Figure S1 X-ray diffraction pattern of Mo:BiVO$_4$ film on SnO$_2$/Si. The blue and red markers

indicate the peaks assigned to tetragonal SnO$_2$ and monoclinic Mo:BiVO$_4$, respectively.
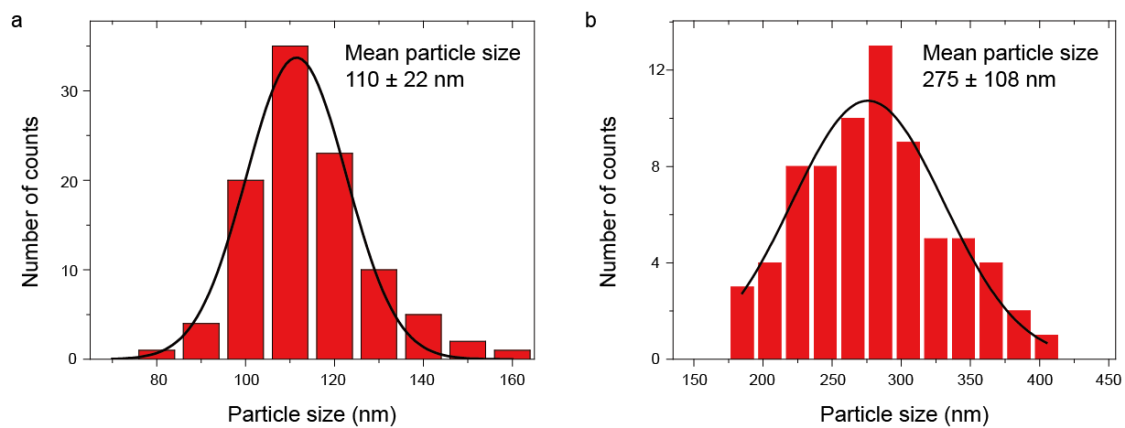

Figure S2 Particle size distribution of the nanoporous (a) and macroporous (b) Mo:BiVO$_4$ electrodes,

obtained from measuring the size of more than 100 particles in SEM images. Black lines represent

fits to a Gaussian function.
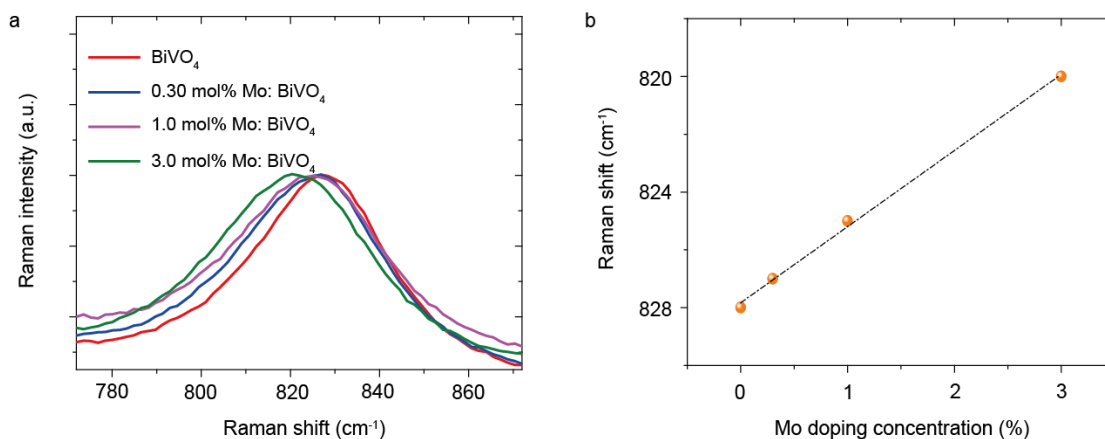
Figure S3 Raman spectra (a) and peak positions (b) of Mo:BiVO$_4$ as a function of the nominal Mo doping level. The V-O stretching mode (at ~828 cm^{-1}) red shifts linearly with the nominal doping level, confirming that Mo is incorporated into the BiVO$_4$ lattice.
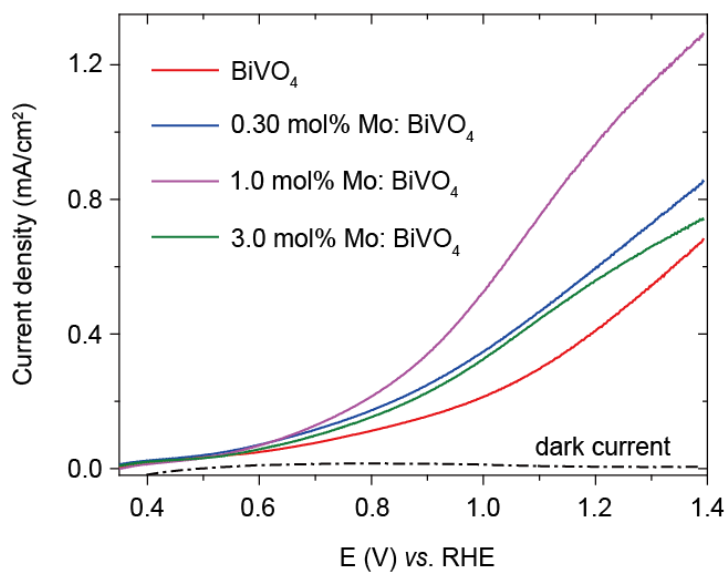
Figure S4 RT photocurrent-voltage characteristics of Mo:BiVO$_4$ photoanodes with different Mo doping concentrations in a 0.5 M phosphate buffer solution (pH 7) under 1sun illumination.
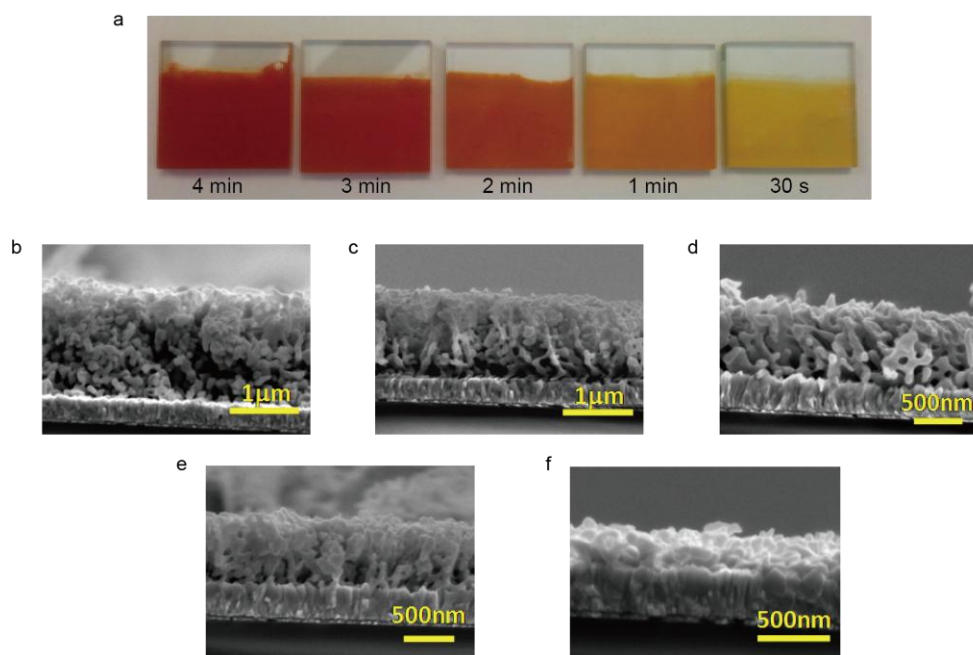
Figure S5 (a) Optical images of as-deposited BiOI on FTO with different deposition time. (b-f)

Cross-sectional SEM images of Mo:BiVO$_4$ on FTO with different BiOI deposition time: (b) 4 min,

(c) 3 min, (d) 2 min, (e) 1 min and (f) 30 s. The average thickness of Mo:BiVO$_4$ film is (b) 1,700 $\pm$

90 nm, (c) 1,190 $\pm$50 nm, (d) 830 $\pm$45 nm, (e) 630 $\pm$36 nm and (f) 260 $\pm$22 nm.
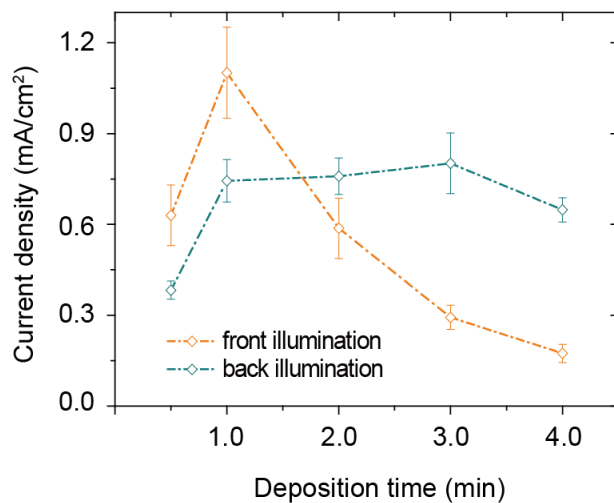
Figure S6 Photocurrent density at 1.23 V *vs*. RHE under front (through the electrolyte) and back (through the transparent contact) illumination (1 sun illumination at RT) as a function of the deposition time of BiOI. The error bar represents a standard deviation of at least three independent measurements.
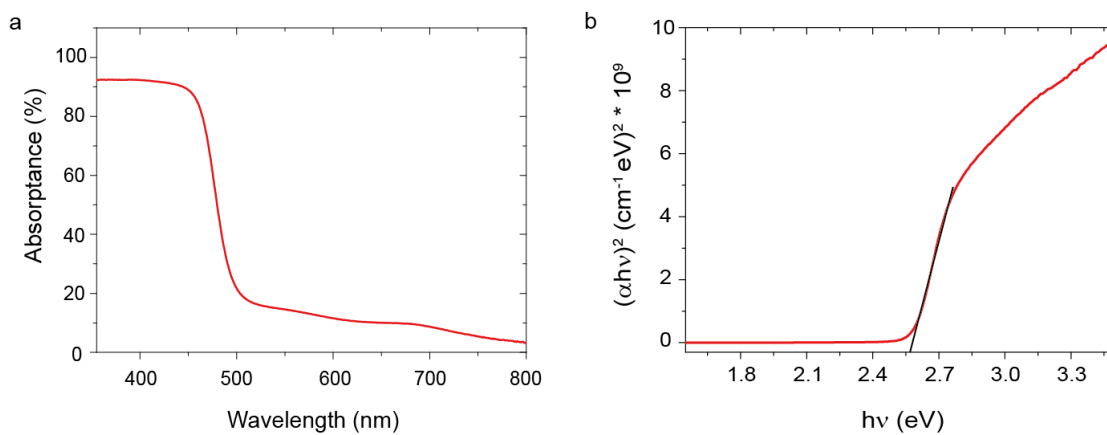

Figure S7 UV-vis spectrum (a) and the corresponding Tauc plot (b) of nanoporous Mo:BiVO$_4$ on FTO with a film thickness of ~630 nm. The bandgap of nanoporous Mo:BiVO$_4$ is estimated to be 2.59 eV.
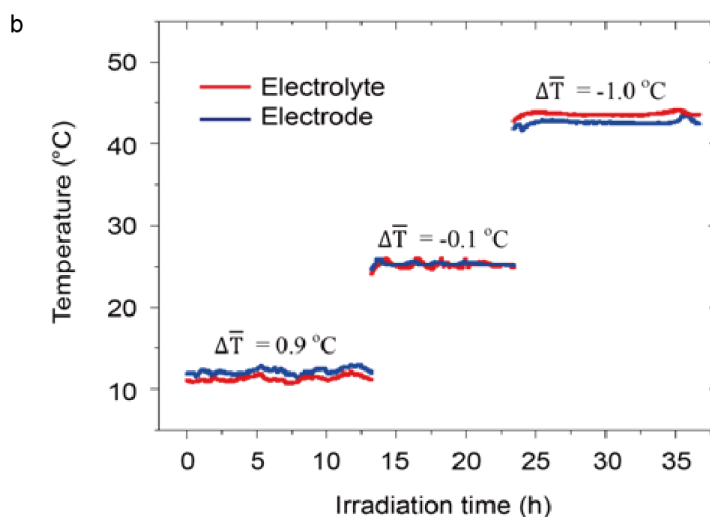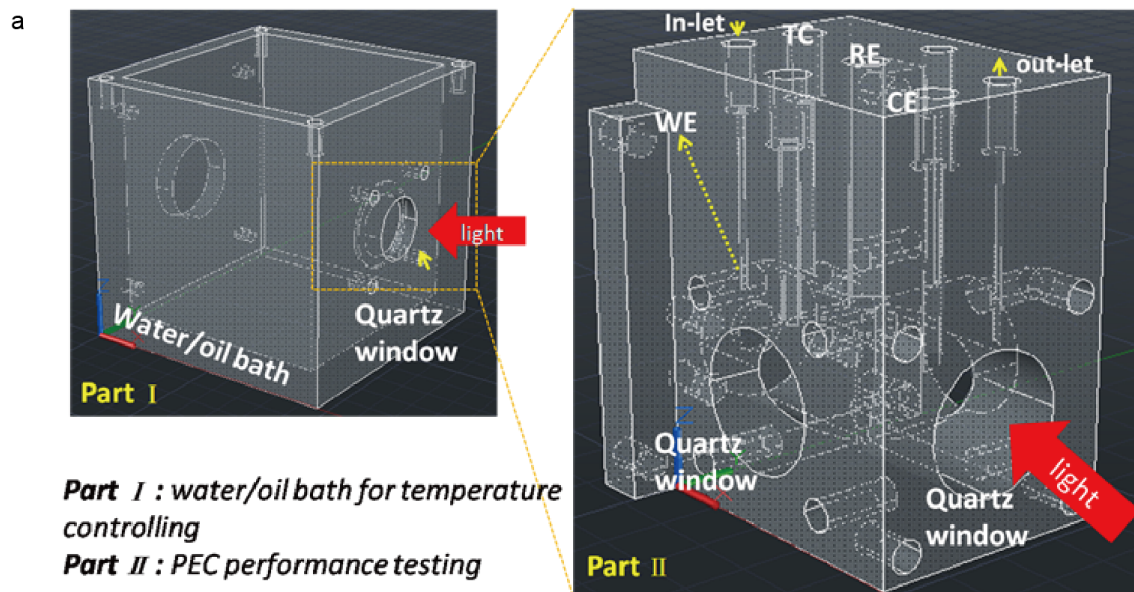
Figure S8 (a) Schematic illustration of the home-made temperature-controlled cell, which was

immersed in a water bath. The cell temperature was measured via a Teflon-coated thermocouple (TC)

located adjacent to the electrode. (b) *In-situ* temperature measurements on electrolyte (red) and

electrode (blue) at different temperature set points under 1 sun irradiation. The average temperature

variations between the electrode and electrolyte were calculated.
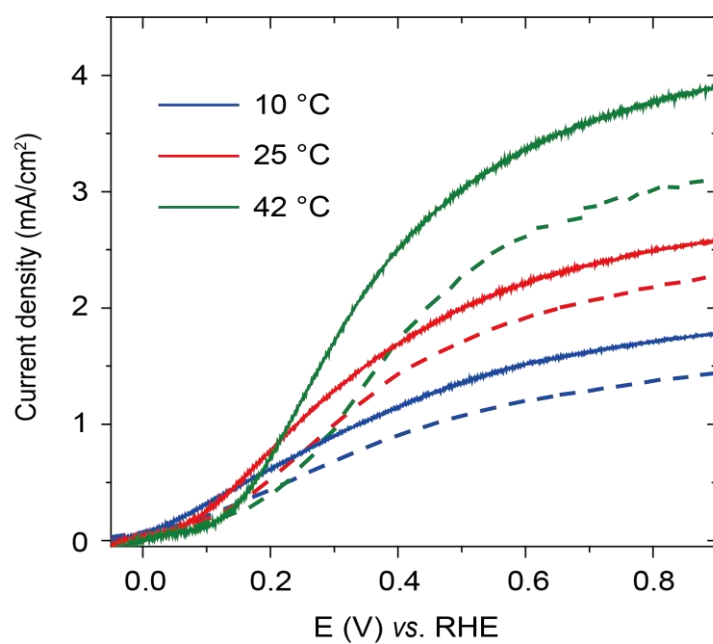
Figure S9 Comparison of temperature-dependent current-voltage curves of CoPi/Mo:BiVO$_4$/SnO$_2$/Si electrode under 1 sun illumination in a 0.5 M phosphate buffer solution (solid lines, pH 7) and a 0.5 M Na$_2$SO$_4$ solution (dashed lines, pH 7).
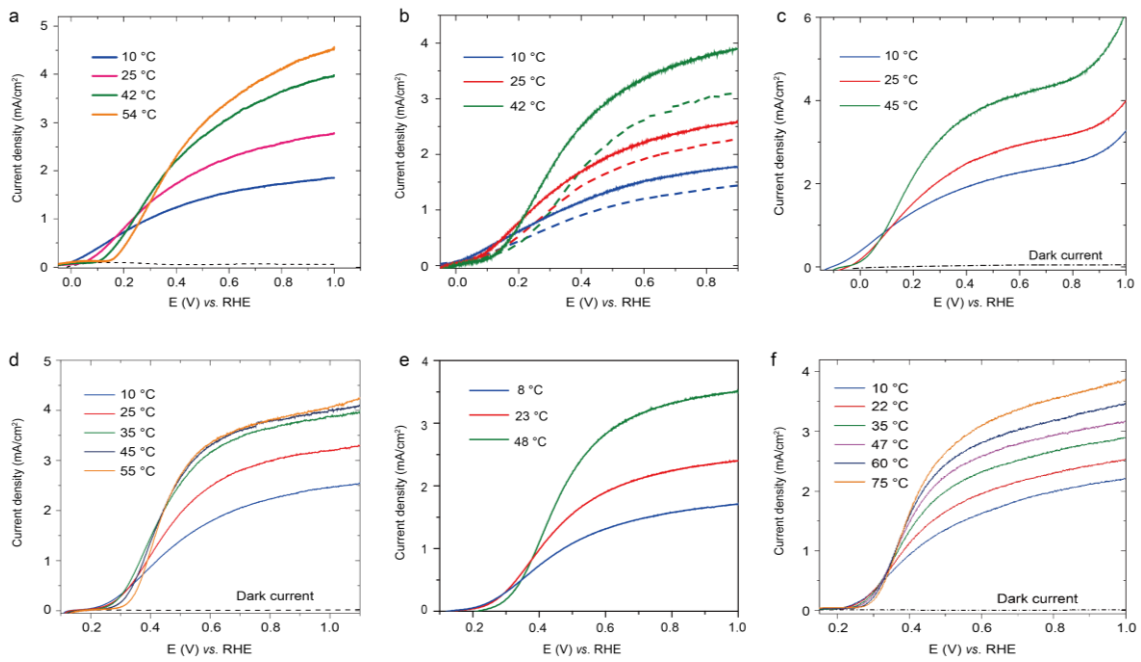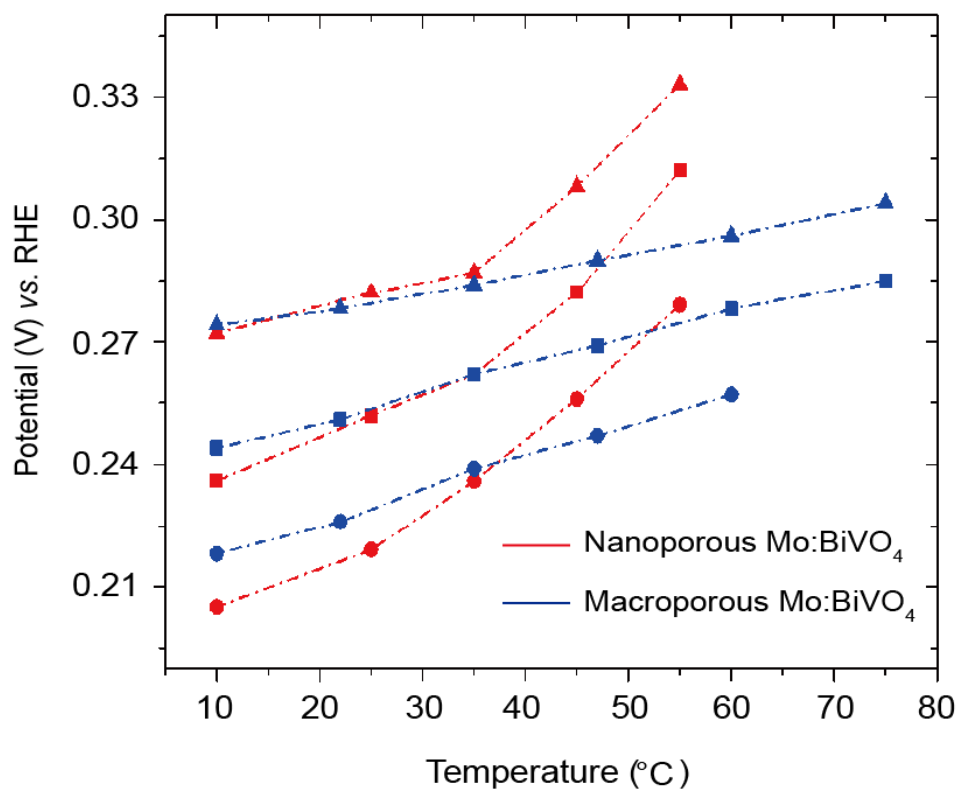
Figure S10 Temperature-dependent photocurrent-voltage curves of CoPi/Mo:BiVO$_4$/SnO$_2$/Si photoanodes under 1 sun illumination in a 0.5 M phosphate buffer solution (a and b, solid lines) and 0.5 M Na$_2$SO$_4$ solution (b, dashed lines). (c) Temperature-dependent photocurrent-voltage curves of Mo:BiVO$_4$/SnO$_2$/Si photoanode under 1 sun illumination in a 0.5 M phosphate buffer solution with 0.1 M Na$_2$SO$_3$ hole scavenger. (d) Temperature-dependent current-voltage curves of nanoporous (d and e) and macroporous (f) Mo:BiVO$_4$ on FTO substrates under 1 sun illumination in a 0.5 M phosphate buffer solution with 0.1 M Na$_2$SO$_3$ hole scavenger.
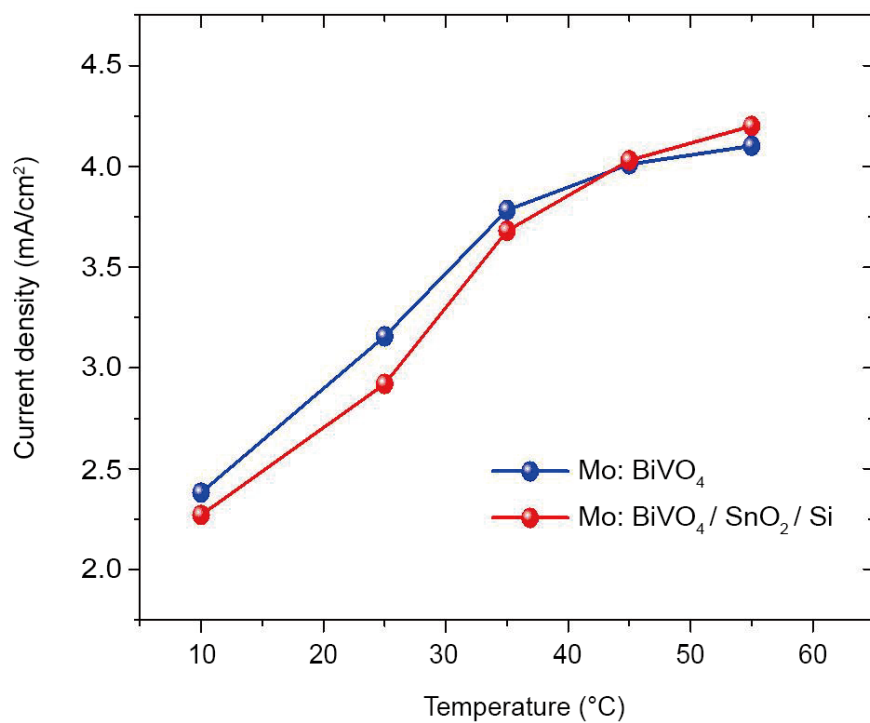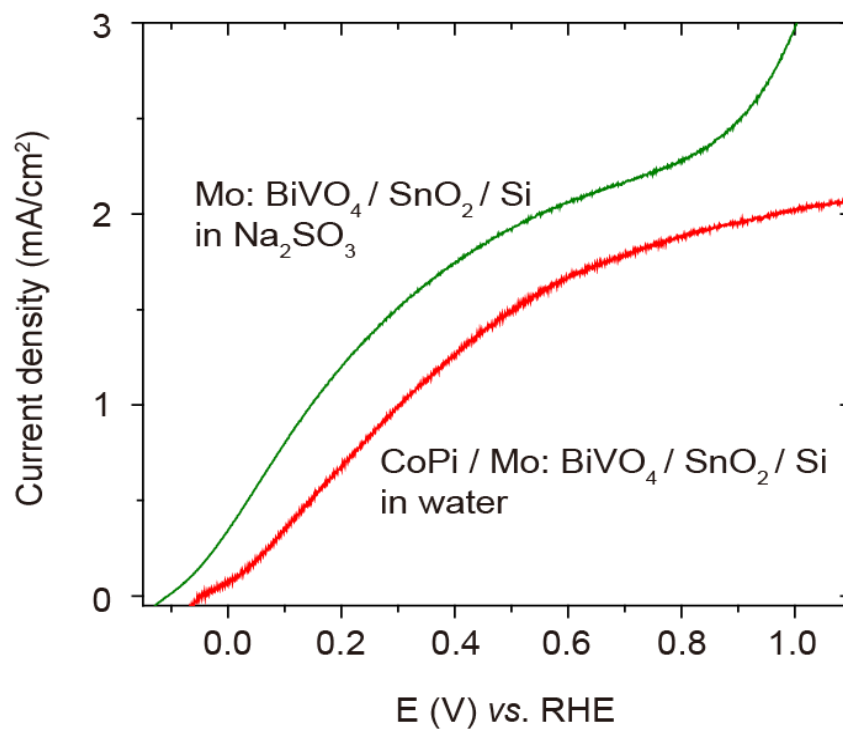
Figure S11 Comparison of the saturation photocurrent evolution as a function of temperature for Mo:BiVO$_4$/SnO$_2$/Si electrode (red, at 0.6 V *vs.* RHE) with Mo:BiVO$_4$ electrode (blue, at 1.0 V *vs.* RHE) in a 0.5 M phosphate buffer solution with 0.1 M Na$_2$SO$_3$ hole scavenger.
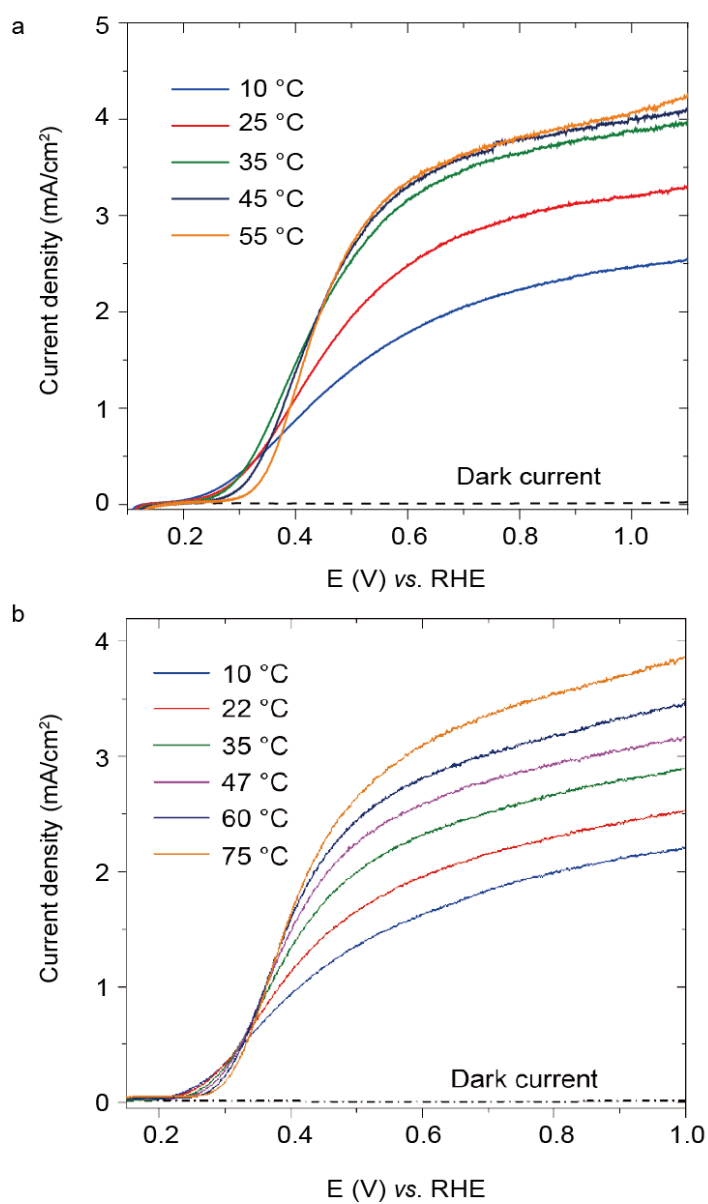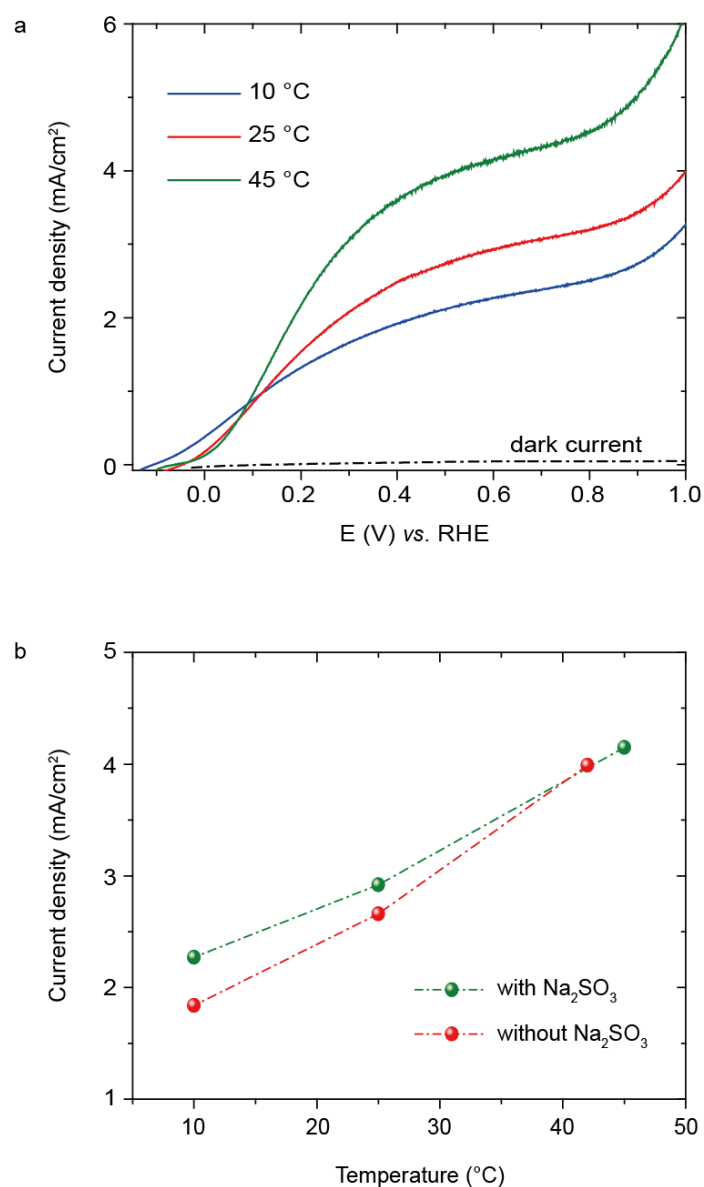
Figure S12 Temperature-dependent current-voltage curves of nanoporous (a) and macroporous (b)

Mo:BiVO$_4$ on FTO substrates under 1 sun illumination in a 0.5 M phosphate buffer solution (pH 7)

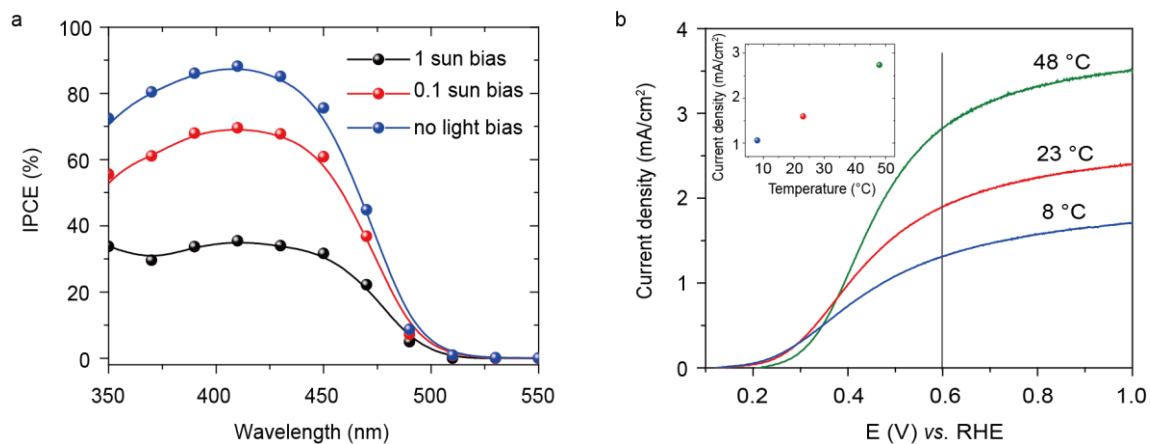with 0.1 M Na$_2$SO$_3$ hole scavenger.

Figure S13 Comparison of the potential, at 0.05 (circle), 0.1 (square) and 0.2 mA/cm^2 (triangle), as a function of temperature for both nanoporous and macroporous electrodes under 1 sun illumination in a 0.5 M phosphate buffer solution (pH 7) with 0.1 M Na$_2$SO$_3$.

Figure S14 Comparison of the photocurrent-voltage characteristics of a CoPi/Mo:BiVO$_4$/SnO$_2$/Si photoanode (red) in a 0.5 M phosphate buffer solution (pH 7) with catalyst-free Mo:BiVO$_4$/SnO$_2$/Si electrode in a 0.5 M phosphate buffer solution with 0.1 M Na$_2$SO$_3$ hole scavenger (green). The measurements were carried out under 1 sun illumination at 10 °C.

Figure S15 (a) Temperature-dependent current-voltage curves of Mo:BiVO$_4$/SnO$_2$/Si electrode under 1 sun illumination in a 0.5 M phosphate buffer solution (pH 7) with 0.1 M Na$_2$SO$_3$ hole scavenger. (b) Comparison of the saturation photocurrent evolution as a function of temperature for CoPi/Mo:BiVO$_4$/SnO$_2$/Si electrode (red, at 1.0 V *vs.* RHE) in a 0.5 M phosphate buffer solution (pH 7) with catalyst-free Mo:BiVO$_4$/SnO$_2$/Si electrode in a 0.5 M phosphate buffer solution with 0.1 M Na$_2$SO$_3$ hole scavenger (green, at 0.60 V *vs.* RHE).

Figure S16 (a) Background light bias-dependent IPCE of nanoporous $Mo:BiVO_4$ film in a 0.5 M phosphate buffer solution (pH 7) with 0.1 M Na_2SO_3 hole scavenger at 0.60 V *vs.*RHE at RT. (b) Temperature-dependent current-voltage curves of $Mo:BiVO_4$ electrode under 1sun illumination in a 0.5 M phosphate buffer solution (pH 7) with 0.1 M Na_2SO_3 hole scavenger. Inset, integrated current density based on the IPCE curves (measured at 0.60 V *vs.* RHE) over all wavelengths under 1 sun light bias at different temperatures.
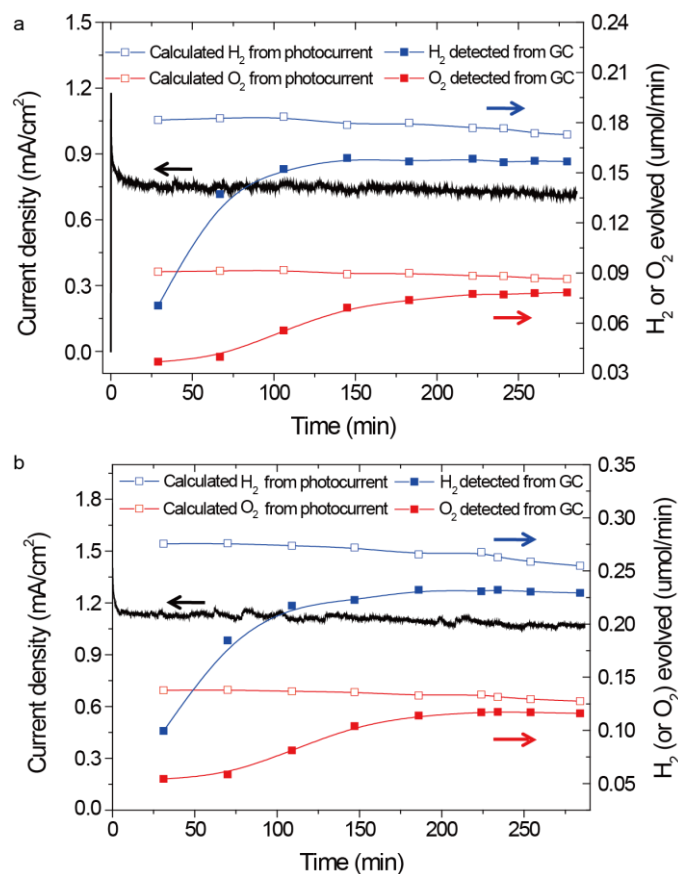
Table S1 Faradaic Efficiency

| Temperature (°C)	Gas from GC	Faradaic efficiency
25	H_2	90 % ± 1 %
	O_2	89 % ± 2 %
42	H_2	89 % ± 1 %
	O_2	90 % ± 1 %

Figure S17 The evolution of H_2 and O_2 gas measured by a gas chromatography under 1 sun illumination at 0.50 V *vs*. RHE in a 0.5 M Na_2SO_4 aqueous solution at 25 °C (a) and 42 °C (b), respectively. The blank squares indicate the calculated H_2 and O_2 generation rate based on the measured photocurrent (black line), assuming 100% Faradaic efficiency. In this flow cell, it takes more than 3 h for H_2 and O_2 to get equilibrium between the liquid and gas phase. The Faradaic efficiency was calculated in the equilibrium stage, which was shown in the **Table S1**.
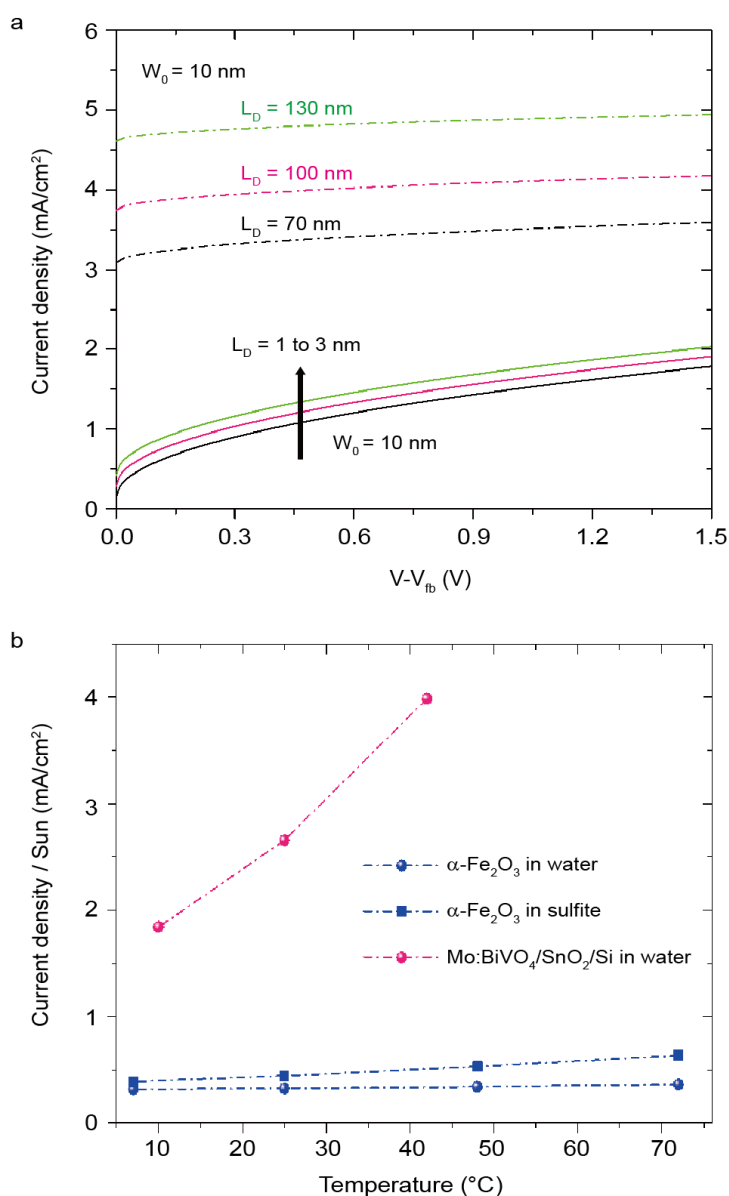
Figure S18 (a) Photocurrent simulation as a function of applied bias. The photocurrent is more sensitive to the minority carrier diffusion length when L_D is much larger than the width of space charge region W_0. (b) Comparison of the saturation photocurrent (at 1.0 V *vs.* RHE on $BiVO_4/SnO_2/Si$, 1.5 V *vs.* RHE on α-Fe_2O_3 for water oxidation and 1.23 V *vs.* RHE for sulfite oxidation) enhancement as a function of temperature. The measurement was taken in a 0.5 M phosphate buffer solution (pH 7) for $BiVO_4$ while in 0.1 M NaOH (pH 13) for α-Fe_2O_3.
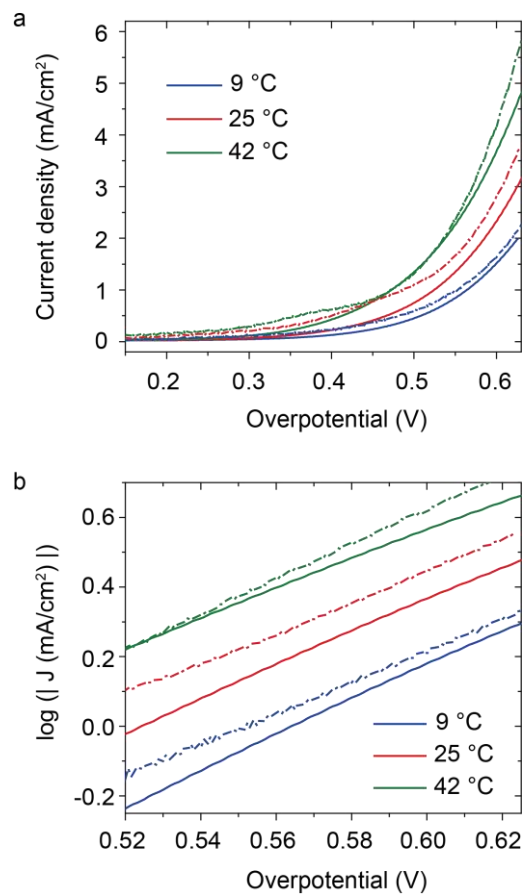
Figure S19 Electrochemical characterization of a CoPi catalyst loaded on FTO (dashed lines) and on Mo:BiVO$_4$/FTO (solid lines) under OER conditions in the dark. Linear sweep voltammograms (a) with a scan rate of 10 mV s^{-1} and Tafel plots (b) as a function of temperature. The variation of the OER equilibrium potential with temperature was accounted for.
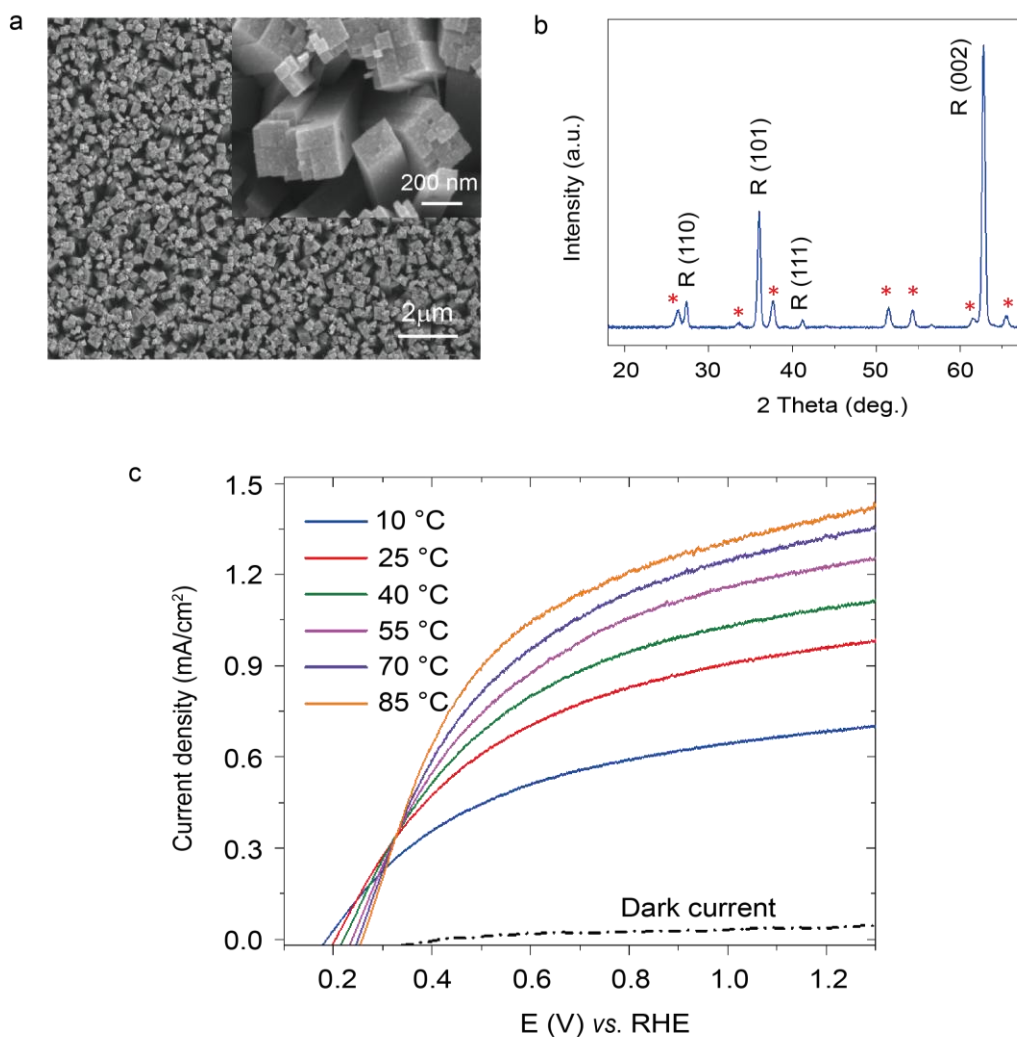
Figure S20 (a) SEM image of vertically aligned TiO_2 nanowire arrays prepared on a FTO substrate.

Inset shows the nanowire morphology in a large magnification. (b) X-ray diffraction pattern of TiO_2

nanowire grown on FTO. The red markers indicate the peaks assigned to FTO. (c)

Temperature-dependent photocurrent-voltage curves of TiO_2/FTO photoanode under 1 sun

illumination in a 1 M NaOH aqueous solution (pH 14). Dark current does not depend significantly

on temperature in the range of 0-1.3 V *vs.* RHE.

Supplementary References

1. Zhong, D. K., Choi, S. & Gamelin, D. R. Near-complete suppression of surface recombination in solar photoelectrolysis by "Co-Pi" catalyst-modified W: BiVO$_4$. *J. Am. Chem. Soc.* **133**, 18370-18377 (2011).

2. Zhong, D. K., Cornuz, M., Sivula, K., Grätzel, M. & Gamelin, D. R. Photo-assisted electrodeposition of cobalt-phosphate (Co-Pi) catalyst on hematite photoanodes for solar water oxidation. *Energy Environ. Sci.* **4**, 1759-1764 (2011).

3. Luo, W. *et al*. Formation energy and photoelectrochemical properties of BiVO$_4$ after doping at Bi^{3+} or V^{5+} sites with higher valence metal ions. *Phys. Chem. Chem. Phys.* **15**, 1006-1013 (2012).

4. Liu, B. & Aydil, E. S. Growth of oriented single-crystalline rutile TiO$_2$ nanorods on transparent conducting substrates for dye-sensitized solar cells. *J. Am. Chem. Soc.* **131**, 3985-3990 (2009).

5. Hwang, Y. J., Hahn, C., Liu, B. & Yang, P. Photoelectrochemical properties of TiO$_2$ nanowire arrays: a study of the dependence on length and atomic layer deposition coating. *ACS Nano* **6**, 5060-5069 (2012).

6. Kanan, M. W. & Nocera, D. G. In situ formation of an oxygen-evolving catalyst in neutral water containing phosphate and Co^{2+}. *Science* **321**, 1072-1075 (2008).

7. Lutterman, D. A., Surendranath, Y. & Nocera, D.G. A self-healing oxygen-evolving catalyst. *J. Am. Chem. Soc.* **131**, 3838-3839 (2009).

8. Jin, J. *et al.* An experimental and modeling/simulation-based evaluation of the efficiency and operational performance characteristics of an integrated, membrane-free, neutral pH solar-driven water-splitting system. *Energy Environ. Sci.* **7**, 3371-3380 (2014).

9. Butler, M. Photoelectrolysis and physical properties of the semiconducting electrode WO$_2$. *J. Appl. Phys.* **48**, 1914-1920 (1977).

10. Kennedy, J. H. & Frese, K. W. Photooxidation of Water at α–Fe$_2$O$_3$ Electrodes. *J. Electrochem. Soc.* **125**, 709-714 (1978).

11. Abdi, F. F., Savenije, T. J., May, M. M., Dam, B. & van de Krol, R. The origin of slow carrier transport in BiVO$_4$ thin film photoanodes: A time-resolved microwave conductivity Study. *J. Phys. Chem. Lett.* **4**, 2752-2757 (2013).

12. Pala, R. A., Leenheer, A. J., Lichterman, M., Atwater, H. A. & Lewis, N. S. Measurement of minority-carrier diffusion lengths using wedge-shaped semiconductor photoelectrodes. *Energy Environ. Sci.***7**, 3424-3430 (2014).

13. Zhong, D. K. & Gamelin, D. R. Photoelectrochemical Water Oxidation by Cobalt Catalyst ("Co−Pi")/α-Fe$_2$O$_3$Composite Photoanodes: Oxygen Evolution and Resolution of a Kinetic Bottleneck. *J. Am. Chem. Soc.* **132**, 4202-4207 (2010).

14. Pilli, S. K. *et al.* Cobalt-phosphate (Co-Pi) catalyst modified Mo-doped BiVO$_4$ photoelectrodes for solar water oxidation. *Energy Environ. Sci.* **4**, 5028-5034 (2011).